ACS APPLIED MATERIALS & INTERFACES

www.acsami.org

Research Article

Ultrahigh Electrical Conductivity in p-Type $CsPbI_2Br$ Perovskite Thin Films by Modulation Doping

Teng Wang,[‖] Jangwoo Ha,[‖] Taejoon Mo, Seung Hwae Heo, Hyein Hwang, Hyunjin Han, Cheol-Joo Kim, Michael D. Dickey, Hyungyu Jin,* and Jae Sung Son*

Cite This: https://doi.org/10.1021/acsami.4c11775

Read Online

ACCESS | Metrics & More | Article Recommendations | Supporting Information

ABSTRACT: The widespread adoption of halide perovskites for application in thermoelectric devices, DC power generators, and lasers is hindered by their low charge carrier concentration. In particular, increasing their charge carrier concentration is considered the main challenge to serve as a promising room-temperature thermoelectric material. Efforts have been devoted to enhancing the charge carrier concentration by doping and composition engineering. However, the coupling between charge carrier concentration and mobility, along with the poor stability of these materials, impedes their development for thermoelectric applications. Herein, we demonstrate the successful increase in the charge carrier concentration of $CsPbI_2Br$ by forming a heterojunction structure with Cu_2S via a facile spin-coating method. The excellent band alignment between two materials combined with a charge-transfer mechanism realizes the modulation doping, resulting in 8 orders of magnitude increase in carrier concentration from 10^{12} to 10^{20} cm^{-3} without detrimental effect on the carrier mobility of $CsPbI_2Br$. The thermoelectric power factor of the heterostructured $CsPbI_2Br$ reached 6.6 $\mu W/m{\cdot}K^2$, which is 330 times higher than that of pristine $CsPbI_2Br$. Furthermore, these films showed higher humidity stability than the control films. This study offers a promising avenue for increasing the charge carrier concentration of halide perovskites, thereby enhancing their potential for various applications.

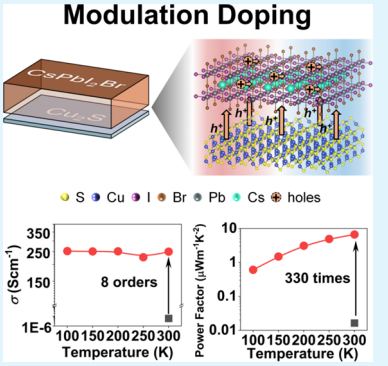

KEYWORDS: *modulation doping, perovskite, Cu_2S, double-layer, heterojunction, thin film*

The remarkable optical and electrical properties of halide perovskites have enabled rapid advancements in photovoltaics, light-emitting diodes, field-effect transistors, and photodetectors.[1,2] The solution processability and low fabrication cost of halide perovskites promote their large-scale production and commercialization. In addition to the above-mentioned rapidly developing areas, emerging applications further boost the potential of halide perovskites.[3,4] To enable such applications, it is, however, important to tune their semiconducting properties, which can be achieved by introducing impurities into the lattice to control the type and concentration of carriers.[5] One strategy for increasing the charge carrier concentration of Pb-based halide perovskites is to vary their composition.[6] However, the increased charge carrier concentration often causes an increase in native defects in the structure that offset any benefits, a phenomenon called the self-compensation effect.[7] Extrinsic doping is another way to increase the charge carrier concentration; Na, Ag, and Sb ions are all possible dopants for methylammonium lead iodide ($MAPbI_3$).[8−10] However, the dopants lead to a low carrier mobility because of the induced additional carrier scattering sources. Higher charge carrier concentrations without detrimental impact on the carrier mobility to further improve the semiconducting properties of halide perovskites are still desired. Relatively high charge carrier concentrations have been reported in Sn-based halide perovskites compared to those in their Pb-based counterparts; however, their poor stability poses challenges for long-term service.[11,12] The development of an efficient and reliable methodology to increase the charge carrier concentration of halide perovskites therefore remains challenging.

Thermoelectric (TE) energy can be used to directly convert heat into electricity. This principle can find applications in environmentally benign cooling and power generation from waste heat.[13] The figure of merit zT is commonly used to evaluate the thermoelectric properties of materials.[14] In detail, $zT = S^2\sigma T/\kappa$, where S, σ, T, and κ are the Seebeck coefficient, electrical conductivity, absolute temperature, and thermal conductivity, respectively.[15] S and σ are interdependent with the charge carrier concentration; increasing charge carrier concentration results in an increase of σ but a decrease of S. So, the optimal values of charge carrier concentration are around $10^{19}-10^{21}$ cm^{-3} for ideal thermoelectric materials.[16] Mean-

Received: July 15, 2024
Revised: September 19, 2024
Accepted: September 22, 2024

while, high carrier mobility, which results in high electrical conductivity, and low thermal conductivity are required to achieve a high zT.[16] It has been demonstrated that strong phonon−phonon interaction of halide perovskites results in an ultralow thermal conductivity of 0.3−0.5 W/m·K, which is lower than most well-studied thermoelectric materials.[17,18] This leads to a theoretical zT exceeding 1 at room temperature, making halide perovskites promising materials for room-temperature TE applications.[19] However, the intrinsically low charge carrier concentration of the Pb-based halide perovskite, which is significantly below the optimal values, hinders the application of this material for TE devices. Considering the self-compensation effect, increasing the charge carrier concentration without reducing the carrier mobility in relatively stable halide perovskites is a key challenge to achieving high TE performance.[20]

Modulation-doped lead-based halide perovskites are promising candidates to overcome this challenge. Modulation doping exploits band alignment of two semiconductors to induce free carriers in one of them.[21,22] As the induced carriers are spatially separated from their parent impurities, modulation-doped semiconductors exhibit high carrier concentration while maintaining unimpaired carrier mobility.[23] Modulation doping is not only commonly used to create a two-dimensional electron gas with high carrier mobility in thin film devices such as field-effect transistors,[24] but it has been proven to be beneficial for TE materials as well.[25,26] However, modulation doping in perovskite films remains largely underexplored.

In this study, we demonstrate the concept of modulation doping in $CsPbI_2Br$ to increase its charge carrier concentration without a detrimental impact on its carrier mobility. Thin films with a heterojunction structure consisting of a top $CsPbI_2Br$ and bottom Cu_2S were successfully fabricated by using the solution-processed spin-coating method, as illustrated in Figure 1. Our results evidence that the charge carrier concentration of

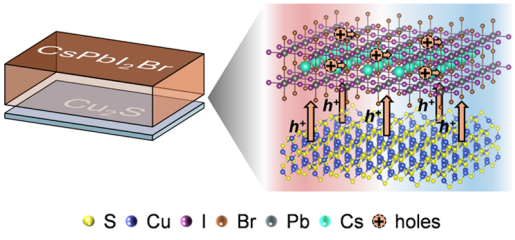

Figure 1. Scheme of the heterostructured $CsPbI_2Br/Cu_2S$ film and the modulation doping mechanism.

the $CsPbI_2Br/Cu_2S$ structure sharply increased as compared to that of the $CsPbI_2Br$ film and could be controlled by adjusting the thickness of the $CsPbI_2Br$ layer, with a value of 10^{21} cm^{-3} achieved when $CsPbI_2Br$ reached a thickness of tens of nanometers. More importantly, the carrier mobility remained unchanged with varying $CsPbI_2Br$ thickness, indicating successful modulation doping in the heterojunction. The low-temperature charge transport properties reveal that the fabricated films exhibit the behavior of typical heavily doped semiconductors with holes as the majority charge carriers, indicating that holes are transferred from Cu_2S to $CsPbI_2Br$. Such a high charge carrier concentration is reflected in the power factor of modulation-doped $CsPbI_2Br$, reaching 6.6 $\mu W/m{\cdot}K^2$, which is 330 times higher than that of pristine $CsPbI_2Br$. Moreover, the fabricated heterostructured thin films maintained their electrical properties for 144 h with a degradation margin of 20%. This study reveals that modulation doping is a promising avenue for optimizing the TE properties of halide perovskites with a high stability.

RESULTS AND DISCUSSION

To realize modulation doping in halide perovskites, it is essential to use both appropriate material combinations and precise heterojunction fabrication techniques. A novel diamine−dithiol solvent mixture has been developed to produce large-scale thin films of various semiconductors, including Cu_2S, Cu_2Se, SnSe, and Sb_2Te_3.[27−29] In this study, Cu_2S was chosen because it enables excellent band alignment with $CsPbI_2Br$ while being readily spin-coated and insoluble in common solvents for halide perovskites such as anhydrous dimethyl sulfoxide (DMSO).[30−32] The film fabrication process is illustrated in Figure 2a. Since the orthogonality of the solvents is crucial for successfully obtaining heterojunctions, the spin-coating method is well-suited for convenient synthesis of them. To fabricate Cu_2S thin films, a Cu_2S molecular precursor solution with a 1:10 vol/vol solvent mixture comprised 1.2-ethanedithiol and ethylenediamine was prepared. The Cu_2S and perovskite double-layer heterostructure thin films were synthesized by first fabricating a Cu_2S layer with a fixed thickness of ∼50 nm by spin-coating and heat treatment at 220 °C and then depositing the perovskite thin film on the Cu_2S by the spin-coating of a precursor prepared from DMSO. The thickness of $CsPbI_2Br$ was controlled by changing the $CsPbI_2Br$ solution concentration.

The X-ray diffraction (XRD) patterns of the $CsPbI_2Br$ and Cu_2S thin films are shown in Figure 2b. Single-layer $CsPbI_2Br$ and Cu_2S thin films spin-coated directly onto glass substrates are denoted as SL-$CsPbI_2Br$ and SL-Cu_2S, respectively. Similarly, the $CsPbI_2Br$ films spin-coated on Cu_2S are denoted as DL(T nm), where T is the total thickness of the double-layer films. XRD patterns reveal the formation of the amorphous phase of SL-Cu_2S and the α phase of SL-$CsPbI_2Br$. The amorphous nature of Cu_2S can be attributed to a lower heat-treatment temperature than the reported minimal annealing temperatures required to achieve crystallinity.[28,33] Meanwhile, three main diffraction peaks at 14.7, 20.8, and 29.7° correspond to (100), (110), and (200) planes of the α phase of $CsPbI_2Br$, respectively.[34] As for DL-$CsPbI_2Br$ films, the intensity of the $CsPbI_2Br$ peaks increases with the thickness, with the thicker films exhibiting typical α phase $CsPbI_2Br$ characteristics. The inconspicuous of the $CsPbI_2Br$ peaks for the DL(97 nm) film did not indicate the absence of $CsPbI_2Br$ crystals, but it was rather caused by the weak signal intensity of the $CsPbI_2Br$ thinnest layers. Scanning electron microscopy (SEM) images clearly confirmed the formation of $CsPbI_2Br$ crystals for all samples as shown in Figure 2c−h, indicating the successful deposition of $CsPbI_2Br$ films onto the Cu_2S layers, irrespective of their thickness. Moreover, the full width at half-maximum of the main peaks for both SL-$CsPbI_2Br$ and DL-$CsPbI_2Br$ were comparable, indicating that $CsPbI_2Br$ films spin-coated on the Cu_2S layers are highly crystalline.

SEM and atomic force microscopy (AFM) were used to study the surface morphologies of SL-$CsPbI_2Br$ and DL-$CsPbI_2Br$ films. Figure 2c,d shows the SEM images of the SL-Cu_2S and SL-$CsPbI_2Br$ films, while Figure 2e−h shows all DL-$CsPbI_2Br$ films. Compared with SL-$CsPbI_2Br$, the DL-$CsPbI_2Br$ films were denser and showed no pinholes or cracks,

https://doi.org/10.1021/acsami.4c11775
ACS Appl. Mater. Interfaces XXXX, XXX, XXX−XXX

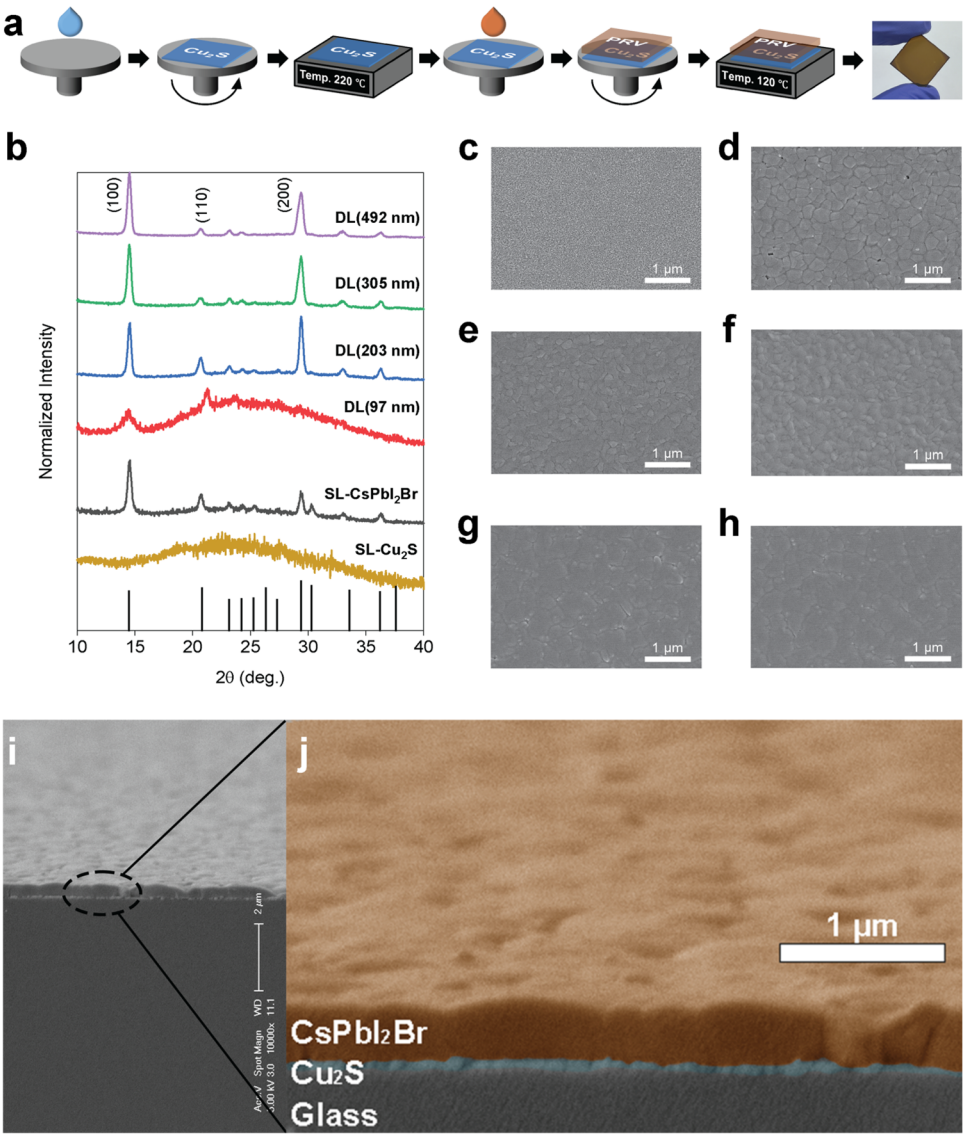

Figure 2. (a) Scheme for the $CsPbI_2Br/Cu_2S$ double-layer film fabrication process. (b) XRD pattern of single-layer Cu_2S, single-layer $CsPbI_2Br$, and double-layer films with different total thicknesses. The bottom black lines are the standard α-phase $CsPbI_2Br$ XRD peaks.[34] SEM images of (c) single-layer Cu_2S, (d) single-layer $CsPbI_2Br$, and (e–h) double-layer films with different total thicknesses. Cross-sectional SEM images under (i) low resolution and (j) high resolution. In panel (j), the $CsPbI_2Br$ layer is marked as a light brown color and the Cu_2S layer is marked as a light blue color.

indicating that $CsPbI_2Br$ fully covered Cu_2S. This result suggests that the formation of $CsPbI_2Br$ films is influenced by the presence of Cu_2S layers during annealing, which is in accordance with previous studies reporting the influence of the substrates on the morphology of Pb-based halide perovskites.[35] The surface roughness of DL-$CsPbI_2Br$ films was measured by AFM, and the values are 1.1, 6.9, 8.8, and 8.9 nm for the 97, 203, 305, and 492 nm thick films, respectively (Figure S1). The flatness of the bottom Cu_2S layer, with an average roughness of 3.1 nm, might be the origin of the low roughness of the $CsPbI_2Br$ films (Figure S1). Additionally, cross-sectional SEM images in Figure 2i,j reveal that the $CsPbI_2Br$ layer is tightly adhered to the Cu_2S layer and displays good crystalline growth. There are no obvious gaps between these two layers, which illustrates well bonding and guarantees effective charge transfer. The full coverage and flatness of the top $CsPbI_2Br$ films ensure that the measured electrical transport properties are attributed to the upper $CsPbI_2Br$ layer rather than the lower Cu_2S layer. These results demonstrate that a high-quality $CsPbI_2Br$ layer was successfully spin-coated onto the Cu_2S layer, suggesting the formation of a $CsPbI_2Br/Cu_2S$ heterojunction structure.

The electrical properties of DL-$CsPbI_2Br$ were measured at room temperature (300 K) as shown in Figure 3. Typically, Pb-based halide perovskites demonstrate exceptionally low σ values owing to their low intrinsic carrier concentration. For instance, the conductivity of both single-crystal and polycrystalline $MAPbI_3$ has been reported to reach as low as 10^{-6} S/cm,[36,37] while that of a $CsPbI_2Br$ film, determined using dark $J-V$ testing, was approximately 10^{-5} S/cm.[38] Consistent with these reported values, σ of SL-$CsPbI_2Br$ is as low as 6×10^{-6} S/cm. Remarkably, the thinnest DL-$CsPbI_2Br$ films (T = 97 nm) exhibit a very high σ of ~250 S/cm, representing an increase of 8 orders of magnitude as compared to SL-$CsPbI_2Br$. As the thickness of $CsPbI_2Br$ films increases, the

https://doi.org/10.1021/acsami.4c11775
ACS Appl. Mater. Interfaces XXXX, XXX, XXX−XXX

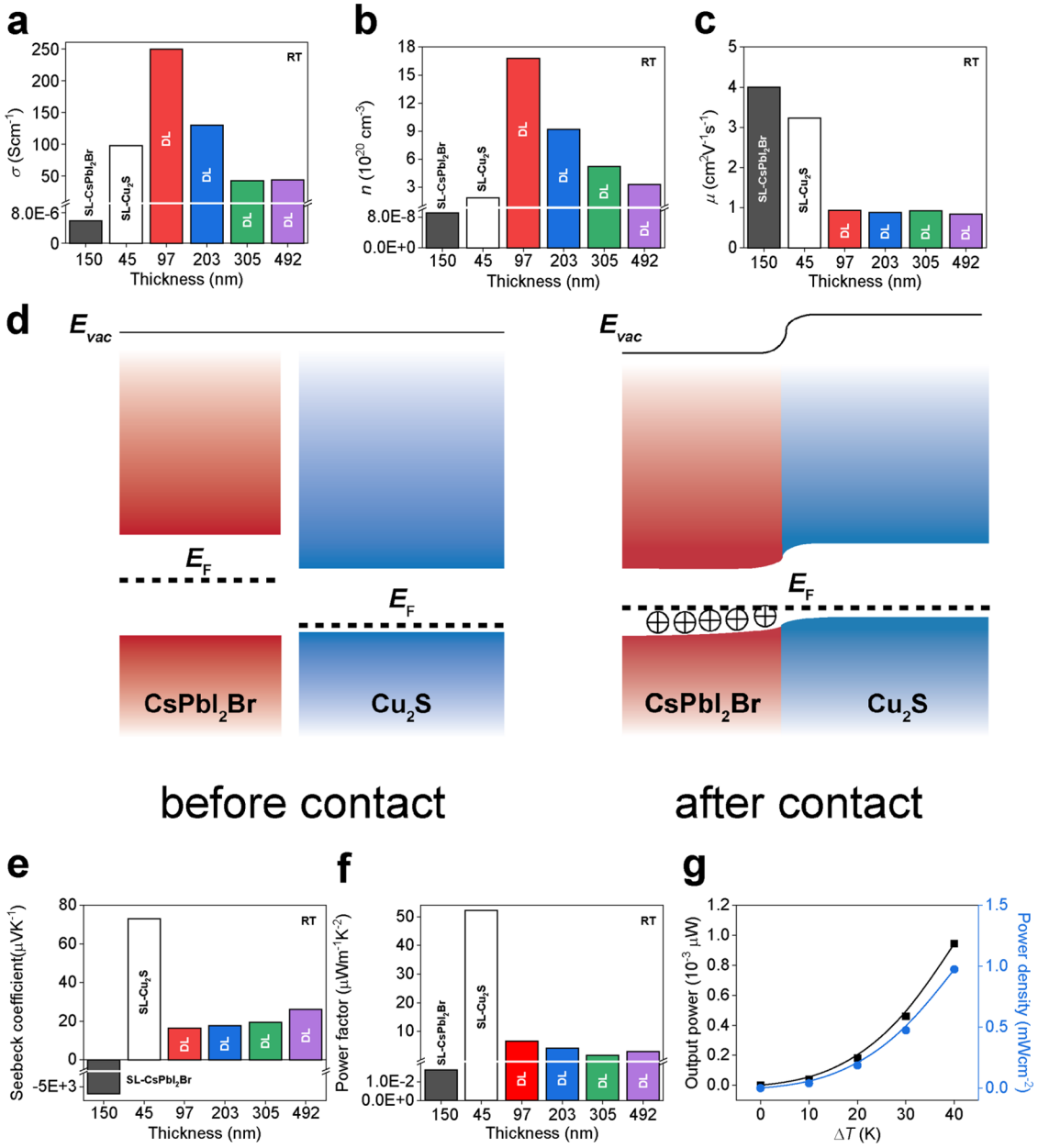

Figure 3. Room-temperature (a) electrical conductivity, (b) carrier concentration, and (c) carrier mobility of single-layer $CsPbI_2Br$, single-layer Cu_2S, and double-layer films with different total thicknesses. (d) Scheme of band alignment of Cu_2S and $CsPbI_2Br$ before and after contact.[30,31] (e) Seebeck coefficient and (f) power factor of single-layer $CsPbI_2Br$, single-layer Cu_2S, and double-layer films with different total thicknesses. (g) Output power and power density of the thermoelectric generator made by DL(97 nm) as a function of temperature difference.

conductivity gradually decreases and stabilizes at ~43 S/cm, still 7 orders of magnitude higher than that of SL-$CsPbI_2Br$.

Hall measurements were performed to determine the charge carrier concentration (n) and mobility (μ) and thereby to better understand the origin of the significant increase in σ observed in DL-$CsPbI_2Br$. As anticipated, n of SL-$CsPbI_2Br$ is relatively low (-9.1×10^{12} cm^{-3}), which is attributed to the self-compensation effect stemming from the formation of localized intrinsic defects, consistent with reported values.[5,7] This low negative n indicates that SL-$CsPbI_2Br$ behaves as a slightly n-type doped semiconductor. Conversely, the DL-$CsPbI_2Br$ films exhibit a significant increase in n, as shown in Figure 3b, reaching levels as high as 10^{21} cm^{-3} and showing a consistently decreasing trend with an increasing total thickness. Furthermore, there is a distinction between the charge carrier types in SL-$CsPbI_2Br$ and DL-$CsPbI_2Br$. The charge carrier concentration changed from negative to positive, indicating that electrons and holes are the primary charge carriers of SL-$CsPbI_2Br$ and DL-$CsPbI_2Br$, respectively. Interestingly, the mobility of the DL-$CsPbI_2Br$ films was approximately 0.9 $cm^2/V{\cdot}s$, regardless of the film thickness, which only represents a marginal reduction from the value of 4.0 $cm^2/V{\cdot}s$ measured for the SL-$CsPbI_2Br$ thin film.

A modulation doping mechanism is proposed to elucidate the significant increase in n, the slight change in μ, and the shift in the carrier type. The schematic depicted in Figure 3d illustrates the modulation concept. Before contact, the Fermi levels of $CsPbI_2Br$ and Cu_2S differ.[30,31] Upon contact, the Fermi levels of both materials equilibrate, causing electrons and holes to diffuse to the Cu_2S and $CsPbI_2Br$ sides,

https://doi.org/10.1021/acsami.4c11775
ACS Appl. Mater. Interfaces XXXX, XXX, XXX−XXX

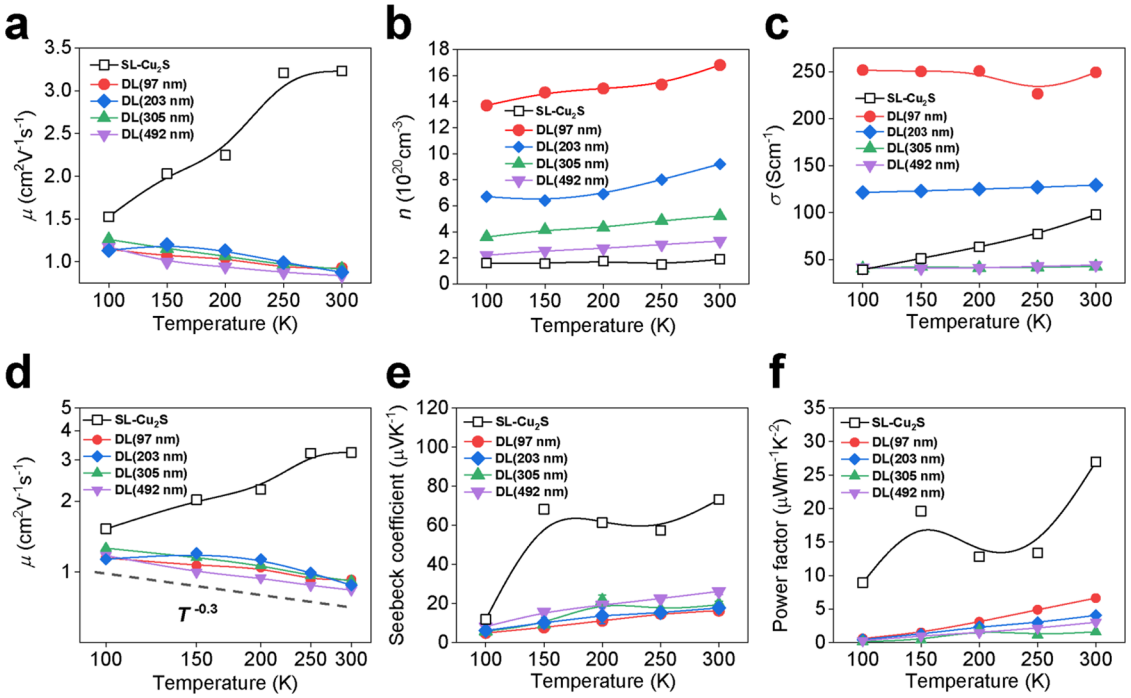

Figure 4. Temperature dependent on (a) electrical conductivity, (b) carrier concentration, (c) carrier mobility, (d) carrier mobility on logarithmic scale, (e) Seebeck coefficient, and (f) power factor of single-layer Cu_2S and double-layer films with different total thicknesses.

respectively. A built-in potential is created when the Fermi levels are equal, and the accumulated holes are located on the $CsPbI_2Br$ side. At the interface between $CsPbI_2Br$ and Cu_2S, the depletion regions are formed on both sides because Cu_2S is a strong p-type semiconductor, whereas $CsPbI_2Br$ is a weak n-type semiconductor. The depletion region on the $CsPbI_2Br$ side is expected to be much wider than that on the Cu_2S side, given the disparity in carrier concentrations, exceeding the thickness of the $CsPbI_2Br$ layer. In detail, the SL-Cu_2S exhibits the characteristic behavior of a heavily doped semiconductor from 100 to 300 K, as illustrated in Figure 4, which is closely associated with the generation of Cu vacancies during the annealing process.[39,40] Owing to the n-type behavior of $CsPbI_2Br$, a significant amount of holes will be injected from Cu_2S to $CsPbI_2Br$. Consequently, this hole injection led to the change in the carrier type from n-type to p-type and a sharp increase in hole concentration, resulting in an extremely high σ.

Additionally, the charge carrier concentration decreased with increasing thickness, indicating a weakening of the modulation doping effect for thicker films, while the mobility of DL-$CsPbI_2Br$ remained unaffected by the thickness. In general, doped semiconductors with high n values exhibit a significantly reduced μ because of impurity scattering caused by the presence of dopant ions.[23] However, the DL-$CsPbI_2Br$ films effectively maintained their μ values despite displaying extremely high values of n. The slight reduction in the mobility in our thin films (Figure 3c) can be attributed to the modulation doping effect by the Cu_2S bottom layer, a phenomenon traditionally reported in heterojunctions. Owing to the difference in Fermi levels, charge carriers diffuse from one material to another.[22] These diffuse carriers are not scattered by the Coulomb force from their parent ionized atoms, thereby ensuring high mobility. The slight reduction of μ in DL-$CsPbI_2Br$ thin films may result from larger carrier−carrier scattering caused by the extremely high charge carrier concentrations. As a result, both the sharply increased n and stable μ are responsible for the extremely high σ of the DL-$CsPbI_2Br$ thin films, which is, to the best of our knowledge, the highest value reported for Pb-based halide perovskites (Table S1).

To further clarify the modulation doping effect on the $CsPbI_2Br$ layer by the Cu_2S layer, the influence of the thickness and the crystallinity of Cu_2S layers on the DL $CsPbI_2Br/Cu_2S$ thin films were investigated. The thickness of the Cu_2S layer was adjusted by spin-coating Cu_2S solutions with varying concentrations of 0.15, 0.20, 0.25, and 0.30 mol/L. The AFM measurements estimated the thickness of the Cu_2S thin films to be 20, 29, 35, and 45 nm, respectively. As expected, the sheet resistance of SL-Cu_2S films shows a pronounced dependence on their thickness, showing that the resistance decreased as the thickness increased (Figure S2). In contrast, the $CsPbI_2Br$ layer in $CsPbI_2Br/Cu_2S$ DL films exhibits nearly identical sheet resistance values regardless of the Cu_2S layer thickness, suggesting that the electrical properties of the $CsPbI_2Br$ thin films are not influenced by the thickness of the Cu_2S layer.

Additionally, to modulate the crystallinity of Cu_2S layers, their annealing temperatures were varied from 200 to 350 °C. As anticipated, elevating the annealing temperature of the Cu_2S layer from 200 to 350 °C resulted in a significant 5-fold increase in electrical conductivity (Figure S3a). Also, Hall measurements revealed that the hole concentration increased by approximately 50 times due to the formation of Cu vacancies at higher annealing temperatures, while the charge carrier mobility decreased, likely due to enhanced defect and carrier−carrier scatterings (Figure S3b), which is consistent with the reported behavior of the Cu_2S.[41] The DL $CsPbI_2Br/Cu_2S$ thin films were then fabricated with the Cu_2S layer annealed at temperatures ranging from 200 to 350 °C. The electrical sheet resistances of these films were measured and compared. In sharp contrast to the properties of Cu_2S, the DL thin films exhibit nearly identical sheet resistances, showing no significant dependence on the annealing temperature of Cu_2S

https://doi.org/10.1021/acsami.4c11775
ACS Appl. Mater. Interfaces XXXX, XXX, XXX−XXX

(Figure S4). To understand this phenomenon, we investigated the band structures of the Cu_2S layers annealed at 200 and 350 °C (conditions expected to produce amorphous and crystalline phases, respectively) using Kelvin probe force microscopy (KPFM) and UV−vis absorption spectroscopy. The work functions (WFs) obtained from the KPFM measurement (Figure S5) indicate no significant difference between the Cu_2S films annealed at 200 and 350 °C. The mean WF values for both samples are approximately 4.5 eV. Furthermore, the band gaps estimated from the Tauc plot analysis of the UV−vis spectra (Figure S6) were nearly identical, approximately 1.24 eV, for both samples. These results demonstrate that the crystallinity of the Cu_2S layer had no significant effect on the band structures of the Cu_2S layer. Therefore, regardless of the annealing temperature of the Cu_2S layer, the modulation doping effect on the $CsPbI_2Br$ layer by Cu_2S is likely to be similar, given the comparable band structures.

These observations indicate that the increased hole concentration and electrical conductivity in the DL thin film were not affected by the thickness and crystallinity of the Cu_2S layer, demonstrating that the electrical properties in the DL thin film originate from the properties of the doped $CsPbI_2Br$ through the modulation doping, rather than the properties of underlying Cu_2S.

To highlight the benefits of halide perovskites with high charge carrier concentrations, we investigated their potential for TE applications. TE parameters, such as S and the power factor (PF), were measured and calculated, as illustrated in Figure 3e,f. A high n value was directly indicated by the S of the DL-$CsPbI_2Br$ films. SL-$CsPbI_2Br$ has an S value of −5158 μV/K (Figure S7), where the negative sign indicates that electrons are the dominant majority carriers, which agrees with the results obtained from the Hall measurements. Generally, S is inversely proportional to n, so the extremely high S of SL-$CsPbI_2Br$ results from its low n.[42] In contrast, the S value of the thinnest DL-$CsPbI_2Br$ films was around +20 μV/K and progressively increased with an increasing thickness. As mentioned previously, the change in the sign of S from negative to positive indicates that the main carriers in $CsPbI_2Br$ changed from electrons to holes. The decrease in S is primarily attributed to the significant increase in the charge carrier concentration, following the reciprocal relationship between S and n. Based on the measured σ and S, a drastic enhancement in PF is evidenced. SL-$CsPbI_2Br$ has a PF value of approximately 0.02 $\mu W/m{\cdot}K^2$, primarily because of its low n. However, by injecting charge carriers through modulation doping, the PF of DL-$CsPbI_2Br$ films experienced a substantial increase, reaching a maximum value of 6.6 $\mu W/m{\cdot}K^2$, which is approximately 330 times higher as compared to the SL-$CsPbI_2Br$ film.

To show the applicability of our DL thin films, we further evaluated the power generation performance of the 97 nm thick DL sample by creating temperature differences across the film, as it exhibited the highest power factor among all of the films. The output power increases with a greater temperature difference, reaching a maximum value of 0.95×10^{-3} μW under the temperature difference of 40 K. The power density of this film reaches 0.97 mW/cm^2. These findings suggest that our modified $CsPbI_2Br$ thin film exhibits significant potential for practical applications. Given the advantages of thin film module fabrication and flexibility, a flexible thermoelectric power generator with high output power density, based on the modified $CsPbI_2Br$, is anticipated.

To gain a deeper understanding of the modulation doping effect on the DL-$CsPbI_2Br$ films, we measured the temperature-dependent electrical and TE transport properties in the range of 100−300 K. As depicted in Figure 4a,b, σ and n exhibit minimal variations with increasing temperature for all DL-$CsPbI_2Br$ films, which is in good agreement with the typical characteristics observed of heavily doped semiconductors. As the total thickness increases, σ decreases and n decreases, indicating a weakened doping effect for thicker $CsPbI_2Br$ films. The temperature-dependent μ consistently decreased for all DL-$CsPbI_2Br$ films. Additionally, it exhibited a characteristic temperature exponent γ of −0.3, as shown in Figure 4d, suggesting an acoustic phonon-dominated mixed scattering mechanism.[43,44] In halide perovskites, carrier mobility is primarily governed by acoustic phonon scattering.[45] Herein, even after doping, this type of scattering remains dominant. Therefore, the injected carriers have a minimal effect on the scattering mechanism, even though they contribute to significantly increasing charge carrier concentration, which confirms the successful achievement of the modulation doping effect. Additionally, the temperature-dependent behavior of μ in DL-$CsPbI_2Br$ significantly differs from that observed in SL-Cu_2S (Figure 4d), indicating that the properties observed for DL-$CsPbI_2Br$ films are characteristic of modulation-doped $CsPbI_2Br$. Measurements and calculations of the temperature-dependent S and PF were also conducted for all of the DL-$CsPbI_2Br$ films. The values of S increase with increasing temperature for all DL-$CsPbI_2Br$ films and show a slight enhancement with the total thickness, which is in agreement with the temperature-dependent behavior of reported TE materials.[46] Owing to the increased S and consistent σ, the value of PF increases with increasing temperature for all DL-$CsPbI_2Br$ films, reaching a maximum value of around 6.6 $\mu W/m{\cdot}K^2$.

In addition to optimizing the electrical and TE properties of $CsPbI_2Br$ through modulation doping, high stability was achieved. The stability characteristics of the SL-$CsPbI_2Br$ and DL-$CsPbI_2Br$ films stored in air at room temperature (300 K) and a relative humidity of 35% were monitored. As shown in Figure 5a, the sheet resistance ($R_{sq.}$) of the DL-$CsPbI_2Br$ film was only 20% higher than its initial value ($R_{0sq.}$) after 144 h. However, a similar increase of $R_{sq.}$ occurred after only 1 h for SL-$CsPbI_2Br$, and $R_{sq.}$ could not be measured after 48 h because of film decomposition, resulting in poor film quality. The increase in $R_{sq.}$ for DL-$CsPbI_2Br$ after 144 h is related to the decomposition of the $CsPbI_2Br$ film. Film decomposition occurred in both SL-$CsPbI_2Br$ and DL-$CsPbI_2Br$, leading to quality deterioration, as illustrated in Figure 5b,c. Nevertheless, the film quality of DL-$CsPbI_2Br$ surpasses that of SL-$CsPbI_2Br$. The absence of cracks and the presence of fewer particles on the surface of the DL-$CsPbI_2Br$ films as compared to that of the SL-$CsPbI_2Br$ films indicate an increased stability. The decomposition of halide perovskites is closely related to the hydration process along grain boundaries because water molecules diffuse faster in these regions.[47] Pinholes present in the SL-$CsPbI_2Br$ films expedite this process, whereas the absence of pinholes for DL-$CsPbI_2Br$ films hinders it. Consequently, the DL-$CsPbI_2Br$ films exhibit greater stability than the SL-$CsPbI_2Br$ films. Moreover, compared with the Sn-based halide perovskites, the stability of DL-$CsPbI_2Br$ is significantly better.[48]

https://doi.org/10.1021/acsami.4c11775
ACS Appl. Mater. Interfaces XXXX, XXX, XXX−XXX

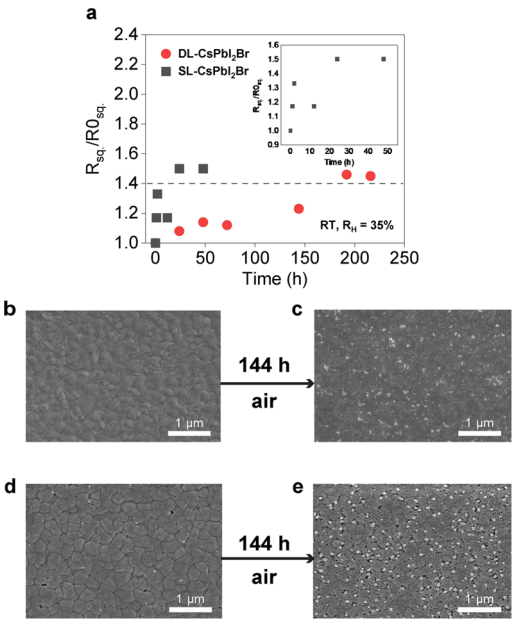

Figure 5. (a) Sheet resistance variation of double-layer and single-layer $CsPbI_2Br$ films compared with their initial value along with time. The figure insider belongs to single-layer $CsPbI_2Br$ films for clear exhibition. SEM images of double-layer films (203 nm) before (b) exposed to air and (c) after 144 h exposed to air. SEM images of single-layer $CsPbI_2Br$ (d) before and (e) after 144 h exposed to air.

CONCLUSIONS

In summary, this study demonstrated the modulation doping effect of $CsPbI_2Br$ by forming heterojunctions with Cu_2S via spin-coating. A several-orders-of-magnitude increase of the electrical conductivity of $CsPbI_2Br$ was achieved, and the mechanism of modulation doping was clarified by analyzing the films' temperature-dependent electrical transport properties. It is evidenced that Cu_2S injects holes into $CsPbI_2Br$ without degrading its mobility, thereby decoupling the charge carrier concentration and mobility. Additionally, the currently developed heterostructured thin films were stable for an extended time duration in ambient conditions owing to the absence of a pinhole on the surface of the films. Modulation doping is a promising avenue for increasing the charge carrier concentration of halide perovskites, thereby paving the way for their large-scale applications in devices requiring high carrier concentrations, such as TE devices. Depending on the concept presented in this work, new material combinations for even precise control of the charge carrier concentrations could be implemented in the future. For example, the modulation doping strategy was successfully applied for different perovskites of formamidinium lead iodide ($FAPbI_3$), which exhibited an electrical conductivity of 5.8 S/cm. This value is ca. 7 orders of magnitude higher than the reported one of $FAPbI_3$.[49] Further development toward the applications of halide perovskites that need high charge carrier concentration is expected.

METHODS

Copper(I) sulfide (Cu_2S, 99.5%, Sigma-Aldrich), cesium bromide (CsBr, 99.999%, Sigma-Aldrich), lead(II) iodide (PbI_2, 99.99%, TCI), 1.2-ethanedithiol ($edtH_2$, >98%, Sigma-Aldrich), ethylenediamine (en, >99.5%, Sigma-Aldrich), and anhydrous dimethyl sulfoxide (DMSO, >99%, Sigma-Aldrich) were used in the experiments as received without further purification.

Soda-lime glass substrates were cleaned by sequential sonication in detergent, deionized water, acetone, isopropyl alcohol, and ethanol for 15 min and dried under a N_2 flow. The substrates were then treated with an O_2 plasma for 30 min. For the synthesis of the Cu_2S thin films, a 0.3 M precursor solution was prepared by dissolving Cu_2S powder in a 10:1 volume ratio of en and $edtH_2$ solvent mixtures. The precursor solution was spin-coated onto soda-lime glass substrates at 6000 rpm for 30 s. The wet films were then annealed at 220 °C for 30 min. Subsequently, the Cu_2S films were cooled to room temperature. For the synthesis of the $CsPbI_2Br$ thin films, precursor solutions of different concentrations were prepared by dissolving a 1:1 molar ratio of CsBr and PbI_2 in DMSO. Since film thickness closely relates to solution viscosity, solution viscosity varies by changing solution concentrations. Thus, the thickness of the films was controlled by changing the solution concentration without changing spin conditions, with higher concentration resulting in thicker films. The precursor solution was spin-coated onto the substrate covered by a Cu_2S layer at 4000 rpm for 120 s. The substrates were then annealed at 50 °C for several minutes, until the film color changed, and then at 120 °C for 10 min to remove the residual organic solvent. This two-step annealing process was necessary to ensure the fabrication of uniform and pinhole-free films. Film synthesis was performed inside a glovebox under a N_2 atmosphere.

The temperature-dependent electrical conductivity, Hall resistivity, and Seebeck coefficient of single-layer Cu_2S and double-layer $CsPbI_2Br/Cu_2S$ films were measured using square samples. For the electrical conductivity and Hall resistivity measurements, the van der Pauw geometry was used with the Cu wires (0.001 in diameter, SPCP-001-50, Omega Engineering, Inc.) connected to the four corners of the square sample using carbon-conductive glue paste (Dupont). A low-frequency AC current (f = 13.7 Hz) was applied through two wires, and the voltage was measured across the remaining two wires using an AC resistance bridge (model 372, Lake Shore Cryotronics, Inc.).[50] DC measurements were also performed for SL-Cu_2S and DL(97 nm) films using a current source (model 6221, Keithley) and a nanovoltmeter (model 2182A, Keithley) with a DC current ranging from 0 to 1 mA. During the Hall measurements, a magnetic field H was swept back and forth between $H = \pm 2$ T. The raw data are shown in Figure S8. Additionally, the difference between the conductance values obtained by AC and DC measurements was within 1% as shown in Figure S9. Seebeck coefficients were measured by using a steady-state method. Two custom T-type thermocouples, made of Cu/Constantan wires (SPCP/SPCI-001−50), were attached to the surface of each sample to determine the temperature difference and the Seebeck voltage. For each wired sample, two resistive heaters were attached to one side of the sample with a heat spreader in between, whereas the opposite side was attached to a BeO pad, serving as a heat sink. Apiezon N grease was applied on both sides of the samples to improve thermal contact. Following the generation of a stable temperature gradient (∇T_x) through the heaters attached to the sample, the hot-side temperature (T_h) and cold-side temperature (T_c) and Seebeck voltages (ΔV_x) were recorded using a nanovoltmeter (model 2182A, Keithley). The room-temperature electrical conductivity and Seebeck coefficient were measured by using a LINSEIS LSR-3 instrument. The room-temperature Hall resistivity of the single-layer $CsPbI_2Br$ was measured using a LINSEIS HCS 1 instrument. The output power was measured with the ceramic heater (10 mm × 10 mm) as a heat source, and the copper plate was used as a heat sink. Temperature differences and voltages were measured with T-type thermocouples connected to the Keithley DMM6500 multimeter. The Tauc plot was obtained by UV−vis absorption spectroscopy (Shimadzu UV-2600 spectrophotometer). The XRD patterns were obtained using a Bruker AXS D8 ADVANCE with Cu Kα radiation under an ambient atmosphere. The microstructure of the thin films was observed by field-emission SEM (FE-SEM; Philips XL30 FEG). The thicknesses were verified using a surface profiler AlphaStep 600 (when thickness higher than 100 nm) and AFM using a Park NX20 system (when thickness less than 100 nm), while the surface roughness was measured by AFM.

https://doi.org/10.1021/acsami.4c11775
ACS Appl. Mater. Interfaces XXXX, XXX, XXX−XXX

■ ASSOCIATED CONTENT

Supporting Information

The Supporting Information is available free of charge at https://pubs.acs.org/doi/10.1021/acsami.4c11775.

Average surface roughness for all samples, room-temperature Seebeck coefficient of SL-$CsPbI_2Br$, and raw data of Hall measurements (PDF)

■ AUTHOR INFORMATION

Corresponding Authors

Hyungyu Jin − *Department of Mechanical Engineering, Pohang University of Science and Technology (POSTECH), Pohang, Gyeongsangbuk-do 37673, Republic of Korea;* orcid.org/0000-0002-0187-0070; Email: hgjin@postech.ac.kr

Jae Sung Son − *Department of Chemical Engineering, Pohang University of Science and Technology (POSTECH), Pohang, Gyeongsangbuk-do 37673, Republic of Korea;* orcid.org/0000-0003-3498-9761; Email: sonjs@postech.ac.kr

Authors

Teng Wang − *Department of Chemical Engineering, Pohang University of Science and Technology (POSTECH), Pohang, Gyeongsangbuk-do 37673, Republic of Korea*

Jangwoo Ha − *Department of Mechanical Engineering, Pohang University of Science and Technology (POSTECH), Pohang, Gyeongsangbuk-do 37673, Republic of Korea*

Taejoon Mo − *Department of Chemical Engineering, Pohang University of Science and Technology (POSTECH), Pohang, Gyeongsangbuk-do 37673, Republic of Korea*

Seung Hwae Heo − *Department of Chemical Engineering, Pohang University of Science and Technology (POSTECH), Pohang, Gyeongsangbuk-do 37673, Republic of Korea*

Hyein Hwang − *Department of Chemical Engineering, Pohang University of Science and Technology (POSTECH), Pohang, Gyeongsangbuk-do 37673, Republic of Korea*

Hyunjin Han − *Department of Chemical Engineering, Pohang University of Science and Technology (POSTECH), Pohang, Gyeongsangbuk-do 37673, Republic of Korea*

Cheol-Joo Kim − *Department of Chemical Engineering, Pohang University of Science and Technology (POSTECH), Pohang, Gyeongsangbuk-do 37673, Republic of Korea;* orcid.org/0000-0002-4312-3866

Michael D. Dickey − *Department of Chemical and Biomolecular Engineering, North Carolina State University, Raleigh, North Carolina 27695, United States;* orcid.org/0000-0003-1251-1871

Complete contact information is available at: https://pubs.acs.org/10.1021/acsami.4c11775

Author Contributions

‖T.W. and J.H. contributed equally to this work. The manuscript was written through contributions of all authors. All authors have given approval to the final version of the manuscript.

Notes

The authors declare no competing financial interest.

■ ACKNOWLEDGMENTS

This work was supported by the National Research Foundation of Korea (NRF) grant funded by the Ministry of Science and ICT (NRF-2022M3H4A1A04076667) and the LG Yonam Foundation of Korea.

■ ABBREVIATIONS

TE, thermoelectric; PF, thermoelectric power factor; XRD, X-ray diffraction; SEM, scanning electron microscopy; AFM, atomic force microscopy; PF, power factor; T_h, hot-side temperature; T_c, cold-side temperature; SL, single-layer; DL, double-layer; $R_{sq.}$, sheet resistance; DMSO, anhydrous dimethyl sulfoxide; $edtH_2$, 1,2-ethanedithiol; en, ethylenediamine

■ REFERENCES

(1) Jena, A. K.; Kulkarni, A.; Miyasaka, T. Halide Perovskite Photovoltaics: Background, Status, and Future Prospects. *Chem. Rev.* **2019**, *119* (5), 3036−3103.

(2) Kim, H.; Han, J. S.; Choi, J.; Kim, S. Y.; Jang, H. W. Halide Perovskites for Applications beyond Photovoltaics. *Small Methods* **2018**, *2* (3), No. 1700310.

(3) Haque, M. A.; Kee, S.; Villalva, D. R.; Ong, W.; Baran, D. Halide Perovskites: Thermal Transport and Prospects for Thermoelectricity. *Adv. Sci.* **2020**, *7* (10), No. 1903389.

(4) Zhou, Y.; Wang, J.; Luo, D.; Hu, D.; Min, Y.; Xue, Q. Recent Progress of Halide Perovskites for Thermoelectric Application. *Nano Energy* **2022**, *94*, No. 106949.

(5) Euvrard, J.; Yan, Y.; Mitzi, D. B. Electrical Doping in Halide Perovskites. *Nat. Rev. Mater.* **2021**, *6* (6), 531−549.

(6) Chen, Y.; Shi, T.; Liu, P.; Xie, W.; Chen, K.; Xu, X.; Shui, L.; Shang, C.; Chen, Z.; Yip, H.-L.; Zhou, G.; Wang, X. The Distinctive Phase Stability and Defect Physics in $CsPbI_2Br$ Perovskite. *J. Mater. Chem. A* **2019**, *7* (35), 20201−20207.

(7) Walsh, A.; Scanlon, D. O.; Chen, S.; Gong, X. G.; Wei, S. Self-Regulation Mechanism for Charged Point Defects in Hybrid Halide Perovskites. *Angew. Chem.* **2015**, *127* (6), 1811−1814.

(8) Yang, Y.; Zou, X.; Pei, Y.; Bai, X.; Jin, W.; Chen, D. Effect of Doping of NaI Monovalent Cation Halide on the Structural, Morphological, Optical and Optoelectronic Properties of $MAPbI_3$ Perovskite. *J. Mater. Sci: Mater. Electron.* **2018**, *29* (1), 205−210.

(9) Chen, Q.; Chen, L.; Ye, F.; Zhao, T.; Tang, F.; Rajagopal, A.; Jiang, Z.; Jiang, S.; Jen, A. K.-Y.; Xie, Y.; Cai, J.; Chen, L. Ag-Incorporated Organic-Inorganic Perovskite Films and Planar Heterojunction Solar Cells. *Nano Lett.* **2017**, *17* (5), 3231−3237.

(10) Huang, L.; Bu, S.; Zhang, D.; Peng, R.; Wei, Q.; Ge, Z.; Zhang, J. Schottky/p-n Cascade Heterojunction Constructed by Intentional n-Type Doping Perovskite Toward Efficient Electron Layer-Free Perovskite Solar Cells. *Sol. RRL* **2019**, *3* (2), No. 1800274.

(11) Liu, T.; Zhao, X.; Li, J.; Liu, Z.; Liscio, F.; Milita, S.; Schroeder, B. C.; Fenwick, O. Enhanced Control of Self-Doping in Halide Perovskites for Improved Thermoelectric Performance. *Nat. Commun.* **2019**, *10* (1), No. 5750.

(12) Wang, T.; Xu, X.; Li, W.; Li, Y.; Liu, Q.; Li, C.; Shan, C.; Li, G.; Shi, T.; Kyaw, A. K. K. Simultaneous Enhancement of Thermoelectric Power Factor and Phase Stability of Tin-Based Perovskites by Organic Cation Doping. *ACS Appl. Energy Mater.* **2022**, *5* (9), 11191−11199.

(13) He, R.; Schierning, G.; Nielsch, K. Thermoelectric Devices: A Review of Devices, Architectures, and Contact Optimization. *Adv. Mater. Technol.* **2018**, *3* (4), No. 1700256.

(14) He, J.; Tritt, T. M. Advances in Thermoelectric Materials Research: Looking Back and Moving Forward. *Science* **2017**, *357* (6358), No. eaak9997.

(15) Wang, T.; Dou, K.; Wang, H.; Kim, J.; Wang, X.; Su, W.; Chen, T.; Kim, W.; Wang, C. Higher-Order Anharmonicity Leads to Ultra-Low Thermal Conductivity and High Output Power Density of SnTe-Based Thermoelectric Materials and Modules. *Mater. Today Phys.* **2022**, *26*, No. 100748.

(16) Jia, N.; Cao, J.; Tan, X. Y.; Dong, J.; Liu, H.; Tan, C. K. I.; Xu, J.; Yan, Q.; Loh, X. J.; Suwardi, A. Thermoelectric Materials and Transport Physics. *Mater. Today Phys.* **2021**, *21*, No. 100519.
(17) Xie, H.; Hao, S.; Bao, J.; Slade, T. J.; Snyder, G. J.; Wolverton, C.; Kanatzidis, M. G. All-Inorganic Halide Perovskites as Potential Thermoelectric Materials: Dynamic Cation off-Centering Induces Ultralow Thermal Conductivity. *J. Am. Chem. Soc.* **2020**, *142* (20), 9553−9563.
(18) Lee, W.; Li, H.; Wong, A. B.; Zhang, D.; Lai, M.; Yu, Y.; Kong, Q.; Lin, E.; Urban, J. J.; Grossman, J. C.; Yang, P. Ultralow Thermal Conductivity in All-Inorganic Halide Perovskites. *Proc. Natl. Acad. Sci. U.S.A.* **2017**, *114* (33), 8693−8697.
(19) He, Y.; Galli, G. Perovskites for Solar Thermoelectric Applications: A First Principle Study of $CH_3NH_3AI_3$ (A = Pb and Sn). *Chem. Mater.* **2014**, *26* (18), 5394−5400.
(20) Bulusu, A.; Walker, D. G. Review of Electronic Transport Models for Thermoelectric Materials. *Superlattices Microstruct.* **2008**, *44* (1), 1−36.
(21) Weidner, M.; Fuchs, A.; Bayer, T. J. M.; Rachut, K.; Schnell, P.; Deyu, G. K.; Klein, A. Defect Modulation Doping. *Adv. Funct. Mater.* **2019**, *29* (14), No. 1807906.
(22) Lashkov, I.; Krechan, K.; Ortstein, K.; Talnack, F.; Wang, S.-J.; Mannsfeld, S. C. B.; Kleemann, H.; Leo, K. Modulation Doping for Threshold Voltage Control in Organic Field-Effect Transistors. *ACS Appl. Mater. Interfaces* **2021**, *13* (7), 8664−8671.
(23) Wang, D.; Li, X.-B.; Sun, H.-B. Modulation Doping: A Strategy for 2D Materials Electronics. *Nano Lett.* **2021**, *21* (14), 6298−6303.
(24) Lee, D.; Lee, J. J.; Kim, Y. S.; Kim, Y. H.; Kim, J. C.; Huh, W.; Lee, J.; Park, S.; Jeong, H. Y.; Kim, Y. D.; Lee, C.-H. Remote Modulation Doping in van Der Waals Heterostructure Transistors. *Nat. Electron.* **2021**, *4* (9), 664−670.
(25) Pei, Y.-L.; Wu, H.; Wu, D.; Zheng, F.; He, J. High Thermoelectric Performance Realized in a BiCuSeO System by Improving Carrier Mobility through 3D Modulation Doping. *J. Am. Chem. Soc.* **2014**, *136* (39), 13902−13908.
(26) Wang, S.-J.; Panhans, M.; Lashkov, I.; Kleemann, H.; Caglieris, F.; Becker-Koch, D.; Vahland, J.; Guo, E.; Huang, S.; Krupskaya, Y.; Vaynzof, Y.; Büchner, B.; Ortmann, F.; Leo, K. Highly Efficient Modulation Doping: A Path toward Superior Organic Thermoelectric Devices. *Sci. Adv.* **2022**, *8* (13), No. eabl9264.
(27) Heo, S. H.; Yoo, J.; Lee, H.; Jang, H.; Jo, S.; Cho, J.; Baek, S.; Yang, S. E.; Gu, D. H.; Mun, H. J.; Oh, M.-W.; Shin, H.; Choi, M. K.; Shin, T. J.; Son, J. S. Solution-Processed Hole-Doped SnSe Thermoelectric Thin-Film Devices for Low-Temperature Power Generation. *ACS Energy Lett.* **2022**, *7* (6), 2092−2101.
(28) Lin, Z.; He, Q.; Yin, A.; Xu, Y.; Wang, C.; Ding, M.; Cheng, H.-C.; Papandrea, B.; Huang, Y.; Duan, X. Cosolvent Approach for Solution-Processable Electronic Thin Films. *ACS Nano* **2015**, *9* (4), 4398−4405.
(29) Webber, D. H.; Brutchey, R. L. Alkahest for V_2VI_3 Chalcogenides: Dissolution of Nine Bulk Semiconductors in a Diamine-Dithiol Solvent Mixture. *J. Am. Chem. Soc.* **2013**, *135* (42), 15722−15725.
(30) Liu, G.; Schulmeyer, T.; Brötz, J.; Klein, A.; Jaegermann, W. Interface Properties and Band Alignment of Cu_2S/CdS Thin Film Solar Cells. *Thin Solid Films* **2003**, *431*−*432*, 477−482.
(31) Yuan, S.; Xian, Y.; Yi, L.; Andreu, C.; Li, W.; Fan, J. Chromium-Based Metal-Organic Framework as A-Site Cation in $CsPbI_2Br$ Perovskite Solar Cells. *Adv. Funct. Mater.* **2021**, *31* (51), No. 2106233.
(32) Jeon, N. J.; Noh, J. H.; Kim, Y. C.; Yang, W. S.; Ryu, S.; Seok, S. I. Solvent Engineering for High-Performance Inorganic-Organic Hybrid Perovskite Solar Cells. *Nat. Mater.* **2014**, *13* (9), 897−903.
(33) Baek, S.; Ban, H. W.; Jeong, S.; Heo, S. H.; Gu, D. H.; Choi, W.; Choo, S.; Park, Y. E.; Yoo, J.; Choi, M. K.; Lee, J.; Son, J. S. Generalised Optical Printing of Photocurable Metal Chalcogenides. *Nat. Commun.* **2022**, *13* (1), No. 5262.
(34) Mali, S. S.; Patil, J. V.; Hong, C. K. Hot-Air-Assisted Fully Air-Processed Barium Incorporated $CsPbI_2Br$ Perovskite Thin Films for Highly Efficient and Stable All-Inorganic Perovskite Solar Cells. *Nano Lett.* **2019**, *19* (9), 6213−6220.
(35) Climent-Pascual, E.; Hames, B. C.; Moreno-Ramírez, J. S.; Álvarez, A. L.; Juarez-Perez, E. J.; Mas-Marza, E.; Mora-Seró, I.; De Andrés, A.; Coya, C. Influence of the Substrate on the Bulk Properties of Hybrid Lead Halide Perovskite Films. *J. Mater. Chem. A* **2016**, *4* (46), 18153−18163.
(36) Xiong, Y.; Xu, L.; Wu, P.; Sun, L.; Xie, G.; Hu, B. Bismuth Doping-Induced Stable Seebeck Effect Based on $MAPbI_3$ Polycrystalline Thin Films. *Adv. Funct. Mater.* **2019**, *29* (16), No. 1900615.
(37) Mettan, X.; Pisoni, R.; Matus, P.; Pisoni, A.; Jaćimović, J.; Náfrádi, B.; Spina, M.; Pavuna, D.; Forró, L.; Horváth, E. Tuning of the Thermoelectric Figure of Merit of $CH_3NH_3MI_3$ (M = Pb, Sn) Photovoltaic Perovskites. *J. Phys. Chem. C* **2015**, *119* (21), 11506−11510.
(38) Wang, A.; Deng, X.; Wang, J.; Wang, S.; Niu, X.; Hao, F.; Ding, L. Ionic Liquid Reducing Energy Loss and Stabilizing $CsPbI_2Br$ Solar Cells. *Nano Energy* **2021**, *81*, No. 105631.
(39) Otelaja, O. O.; Ha, D.-H.; Ly, T.; Zhang, H.; Robinson, R. D. Highly Conductive $Cu_{2-x}S$ Nanoparticle Films through Room-Temperature Processing and an Order of Magnitude Enhancement of Conductivity via Electrophoretic Deposition. *ACS Appl. Mater. Interfaces* **2014**, *6* (21), 18911−18920.
(40) He, Y.; Day, T.; Zhang, T.; Liu, H.; Shi, X.; Chen, L.; Snyder, G. J. High Thermoelectric Performance in Non-Toxic Earth-Abundant Copper Sulfide. *Adv. Mater.* **2014**, *26* (23), 3974−3978.
(41) Liu, L.; Zhou, B.; Deng, L.; Fu, W.; Zhang, J.; Wu, M.; Zhang, W.; Zou, B.; Zhong, H. Thermal Annealing Effects of Plasmonic $Cu_{1.8}S$ Nanocrystal Films and Their Photovoltaic Properties. *J. Phys. Chem. C* **2014**, *118* (46), 26964−26972.
(42) Lee, K. H.; Kim, S.; Kim, H.-S.; Kim, S. W. Band Convergence in Thermoelectric Materials: Theoretical Background and Consideration on Bi-Sb-Te Alloys. *ACS Appl. Energy Mater.* **2020**, *3* (3), 2214−2223.
(43) Shuai, J.; Mao, J.; Song, S.; Zhu, Q.; Sun, J.; Wang, Y.; He, R.; Zhou, J.; Chen, G.; Singh, D. J.; Ren, Z. Tuning the Carrier Scattering Mechanism to Effectively Improve the Thermoelectric Properties. *Energy Environ. Sci.* **2017**, *10* (3), 799−807.
(44) Liu, Z.; Mao, J.; Peng, S.; Zhou, B.; Gao, W.; Sui, J.; Pei, Y.; Ren, Z. Tellurium Doped N-Type Zintl $Zr_3Ni_3Sb_4$ Thermoelectric Materials: Balance between Carrier-Scattering Mechanism and Bipolar Effect. *Mater. Today Phys.* **2017**, *2*, 54−61.
(45) Chin, X. Y.; Cortecchia, D.; Yin, J.; Bruno, A.; Soci, C. Lead Iodide Perovskite Light-Emitting Field-Effect Transistor. *Nat. Commun.* **2015**, *6* (1), No. 7383.
(46) Feng, J.; Li, J.; Liu, R. Low-Temperature Thermoelectric Materials and Applications. *Nano Energy* **2024**, *126*, No. 109651.
(47) Zhang, C.; Shen, T.; Guo, D.; Tang, L.; Yang, K.; Deng, H. Reviewing and Understanding the Stability Mechanism of Halide Perovskite Solar Cells. *InfoMat* **2020**, *2* (6), 1034−1056.
(48) Chung, I.; Song, J.-H.; Im, J.; Androulakis, J.; Malliakas, C. D.; Li, H.; Freeman, A. J.; Kenney, J. T.; Kanatzidis, M. G. $CsSnI_3$: Semiconductor or Metal? High Electrical Conductivity and Strong Near-Infrared Photoluminescence from a Single Material. High Hole Mobility and Phase-Transitions. *J. Am. Chem. Soc.* **2012**, *134* (20), 8579−8587.
(49) Han, Q.; Bae, S.; Sun, P.; Hsieh, Y.; Yang, Y.; Rim, Y.; Zhao, H.; Chen, Q.; Shi, W.; Li, G.; Yang, Y. Single Crystal Formamidinium Lead Iodide ($FAPbI_3$): Insight into the Structural, Optical, and Electrical Properties. *Adv. Mater.* **2016**, *28* (11), 2253−2258.
(50) Qiao, W.; Zhao, J.; Chen, Y.; Cao, S.; Xing, W.; Cai, R.; Guo, L.; Qian, T.; Xie, X. C.; Han, W. Observation of Quasi-Two-Dimensional Superconductivity at the EuO-$BaBiO_3$ Interface. *Phys. Rev. B* **2024**, *109* (5), No. 054509.

https://doi.org/10.1021/acsami.4c11775
ACS Appl. Mater. Interfaces XXXX, XXX, XXX−XXX